



# Insights into the surface-defect dependence of molecular oxygen activation over birnessite-type MnO<sub>2</sub>

Wenjuan Yang<sup>a,b</sup>, Yongfa Zhu<sup>a,\*</sup>, Fei You<sup>c</sup>, Long Yan<sup>b</sup>, Yajun Ma<sup>b</sup>, Cuiying Lu<sup>b</sup>, Pingqiang Gao<sup>b</sup>, Qiang Hao<sup>d</sup>, Wenlu Li<sup>a</sup>

<sup>a</sup> Department of Chemistry, Tsinghua University, Beijing, 100084, China

<sup>b</sup> School of Chemistry and Chemical Engineering, Yulin University, Yulin City, 719000, Shaanxi, China

<sup>c</sup> School of Mathematics and Statistics, Yulin University, Yulin City, 719000, Shaanxi, China

<sup>d</sup> School of Materials Science and Technology, China University of Geosciences, Beijing 100083, China

## ARTICLE INFO

### Keywords:

MnO<sub>2</sub>  
Crystal surface potential  
Superoxide  
Peroxide  
DFT

## ABSTRACT

In establishing the kinetics, energetics and mechanisms of phenolic degradation reactivity, active reactive oxygen species (ROS) on catalysts surface could exert a vital part. This paper attempts to account for different ROS at the atomic level using octahedral layered birnessite-type MnO<sub>2</sub> as a platform with different crystal planes which could induce the Jahn-Teller effect and further realize deep mineralization of phenolic pollutants at low temperature. The catalytic degradation phenol rate of (100) MnO<sub>2</sub> is 3 times as much as that of (001) MnO<sub>2</sub>, and the activation energy of the catalytic reaction is reduced by 11 KJ/mol. The degradation content of (100) MnO<sub>2</sub> surpasses 30% than that of (001) MnO<sub>2</sub>. Both spin-trapping EPR and DFT results show superoxide ( $\cdot\text{O}_2^-$ ) species could exist on (001) MnO<sub>2</sub> through one electron transfer, while the peroxide ( $\text{O}_2^{2-}$ ) species exist on (100) MnO<sub>2</sub> via two electrons transfer. All the results illustrate that birnessite MnO<sub>2</sub> possesses surface-dependent molecular oxygen activation properties.

## 1. Introduction

Molecular oxygen activation is extremely vital to understand the interaction between oxygen gas and catalyst surfaces, further produce reactive oxygen species (ROS). Two types of ROS have been identified via materials characterization techniques and electronic-structure computations: electrophilic species (superoxide ( $\cdot\text{O}_2^-$ ) or peroxide ( $\text{O}_2^{2-}$ )) and nucleophilic species (lattice oxygen and terminal or bridging oxygen groups). Especially, electrophilic species could determine the catalytic activity, while nucleophilic species largely resolve catalytic selectivity. In redox-type reactions, the crucial steps are the uptake of substrate oxygen atoms into reactants adsorbed on a substrate and the replenishing of the vacancies created by dissociating oxygen molecules delivered from the gas phase. This Mars-van Krevelen mechanism of molecule O<sub>2</sub> activation is generally accepted for CeO<sub>2</sub>, V<sub>2</sub>O<sub>3</sub>, BiOCl and TiO<sub>2</sub>. The research about O<sub>2</sub> and oxygen vacancy is hot spot and corner stone in international scientific field, which is continues to be intensely debated. Erik Wahlström et al. observe the electron transfer-induced dynamics of oxygen molecules on the TiO<sub>2</sub>(110) surface by time-resolved scanning tunneling microscopy. The result show that the O<sub>2</sub> hopping rate depend on the

number of oxygen vacancies, which determines the density of conduction band electrons [1]. O<sub>2</sub> adsorbed as superoxo ( $\cdot\text{O}_2^-$ ) at five-fold-coordinated Ti sites was transformed to peroxo ( $\text{O}_2^{2-}$ ) via reaction with an oxygen vacancy (V<sub>O</sub>) based on DFT by Martin Setvín [2]. Hou J. G. et al. directly verify the exact adsorption sites and the dynamic behaviors of molecular O<sub>2</sub> on the reduced rutile TiO<sub>2</sub>(110) surface using an *in situ* O<sub>2</sub> dosing method by scanning tunneling microscopy [3]. In the experimental spectroscopic characterization, the identification of electrophilic species  $\cdot\text{O}_2^-$  and  $\text{O}_2^{2-}$  species are based on the fingerprints of electron paramagnetic resonance (EPR), IR and Raman spectra (1015–1150 cm<sup>-1</sup> for  $\cdot\text{O}_2^-$  species, and 850–950 cm<sup>-1</sup> for  $\text{O}_2^{2-}$ ) [4]. These experimental results also motivated the relevant theoretical study of ROS. In theoretical calculations,  $\cdot\text{O}_2^-$  and  $\text{O}_2^{2-}$  species are mainly distinguished by the O–O bond length ( $\text{O}_2^{2-}$  (O–O: 1.44 Å) and  $\cdot\text{O}_2^-$  (O–O: 1.33 Å)) and charge number in the outermost layer orbital [5]. The electronic configuration of the paramagnetic  $\cdot\text{O}_2^-$  and diamagnetic species  $\text{O}_2^{2-}$  should be just one unpaired electron and one paired electrons, respectively. In the process of generating ROS, Gerischer et al. showed that the rate of electron transfer to adsorbed O<sub>2</sub> limits the overall quantum efficiency rather than the diffusion of O<sub>2</sub> on large TiO<sub>2</sub>

\* Corresponding author.

E-mail address: [zhuyf@mail.tsinghua.edu.cn](mailto:zhuyf@mail.tsinghua.edu.cn) (Y. Zhu).

<https://doi.org/10.1016/j.apcatb.2018.03.107>

Received 14 January 2018; Received in revised form 27 March 2018; Accepted 29 March 2018

Available online 29 March 2018

0926-3373/ © 2018 Elsevier B.V. All rights reserved.

particles [6]. Moreover, kinetics experiments and calculations have demonstrated that  $O_2$  is not efficient as an electron scavenger and may limit the overall catalytic rate [7]. Activating  $O_2$  into electrophilic superoxide ( $\cdot O_2^-$ ), peroxide ( $O_2^{2-}$ ) or ( $\cdot O_4^{2-}$ ) species is dependent on many factors such as the  $O_2$  gas coverage, oxygen vacancy atomic structure, its location and so on. [8–13] Tilocca et al. points out that  $O_2$  could adsorb on the oxygen vacancy with its axis parallel to the  $TiO_2$  (110) plane in the form of  $O_2^{2-}$  [14], which was sequent proved by Tan et al. through the observation of STM [15]. Aschauer et al. found that  $O_2$  would generate into  $O_2^{2-}$  when the ratio of the amount of adsorbed  $O_2$  to oxygen vacancy is less than or equals 1:1. While  $O_2$  would generate into  $\cdot O_2^-$  when the ratio of the amount of adsorbed  $O_2$  to oxygen vacancy is more than 1.5:1.26. Nevertheless, there were almost no relevant research of the reaction between  $O_2$  and oxygen vacancy of birnessite-type  $MnO_2$  in the experimental and theoretical method. Furthermore, the corresponding electronic transfer mechanism between  $MnO_2$  and  $O_2$  as well as the catalytic reactive oxygen active species like  $\cdot O_2^-$  and  $O_2^{2-}$  of the  $MnO_2$ -based catalyst were seldom reported, which is worthy to be further investigated.

In order to deep mineralization of phenol at low temperature, manganese dioxide attracts great attention owing to its intense oxidation capacity, tunnel effect and catalytic characteristic [16,17]. Moreover,  $MnO_2$  has many crystalline structures, such as  $\alpha$ - $MnO_2$ ,  $\beta$ - $MnO_2$ ,  $\gamma$ - $MnO_2$ ,  $\delta$ - $MnO_2$ ,  $\lambda$ - $MnO_2$ ,  $\eta$ - $MnO_2$ ,  $\epsilon$ - $MnO_2$ . [18–20] In a series of manganese dioxide crystal, birnessite ( $\delta$ - $MnO_2$ ) is a common structure with a two-dimensional layered structure. Due to their unique properties, such as mixed valence states ( $3+$ ,  $4+$ ), and easy release of lattice oxygen,  $\delta$ - $MnO_2$  catalytic materials have been widely used in catalytic oxidation of organic pollutants, water oxidation catalysis and other fields. Defect engineering is regarded as an effective way to tune catalytic reaction kinetics, activation energetics and reactive mechanisms. [21–27] These deficiencies sites worked as active sites are capable of accommodating electronic states of adsorbents *via* the surface dangling bonds and localized electrons. The catalytic activity depends on the number of surface active sites. The relationship between the shape/crystal plane effect and the surface active sites is therefore a very important link between the structures and properties. When birnessite-type  $MnO_2$  suffers from  $H_2$  reduction or vacuum annealing, the surface vacancy would easily form along with  $Mn^{4+}$  ions reducing to  $Mn^{3+}$ . Sakai et al. firstly reported photocurrent generation by  $MnO_2$  with  $\sim 3$  mol% Mn vacancy [28]. Ceder et al. directly visualized the Jahn–Teller effect in  $Na_{5/8}MnO_2$  with Na vacancy [29]. Kwon et al. reported Ruetschi defect (Mn vacancy) induced photoconductivity in layered  $MnO_2$  by density functional theory (DFT) study [30]. Zhang et al. reported birnessite-type  $MnO_2$  with Mn vacancy favors room-temperature oxidation of formaldehyde in the atmosphere [8]. Single-layer  $MnO_2$  nanosheet with Mn and/or O vacancies was manifested to present half-metallic character, which is dissimilar from their bulk counterparts by Xie et al. [7] Mn vacancy survey is dominant, while oxygen vacancy investigation is sluggish but inevitable. Deeply probing the role and structure of oxygen vacancies in  $MnO_2$  is open in the air but worthy to be investigated.

In this manuscript, birnessite-type  $MnO_2$  with (001) and (100) crystal planes were successfully experimentally fabricated. The Raman spectrum and High-Resolution Transmission Electron Microscopy (HRTEM) of  $MnO_2$  were characterized to identify the chemical bond information and exposed crystal planes. The catalytic degradation phenol rate of (100)  $MnO_2$  is 3 times faster than that of (001)  $MnO_2$  with the activation energy decreasing by 11 KJ/mol. Mineralization content of (100)  $MnO_2$  exceeds 30% than that of (001)  $MnO_2$ . EPR technique was carried out to detect the active species such as superoxide radical ( $\cdot O_2^-$ ) and peroxide radical ( $O_2^{2-}$ ) of  $MnO_2$  catalyst, which is in agreement with DFT calculation results.

## 2. Experiment part

### 2.1. Catalyst preparation

All chemicals used for the preparation were of analytical grade. 1.0 g of  $KMnO_4$  and 0.15 g  $MnSO_4 \cdot H_2O$  were dissolved into 70 mL deionized water. Then, the solution was transformed into a hydrothermal reactor and was kept at the temperature of 200 °C for 12 h. After the reactor was cooled down to room temperature, the precipitate was centrifuged and then washed several times with deionized water. The precipitate was dried at 105 °C for 24 h and then calcined in a muffle furnace under 300 °C for 3 h. The as-obtained sample was denoted as (001)  $MnO_2$ .

Birnessite  $MnO_2$  (100) crystal plane samples were synthesized as follows: 1.0 g of  $KMnO_4$  and 0.4 g  $(NH_4)_2C_2O_4 \cdot H_2O$  were dissolved in 130 mL of deionized water in a round-bottom flask placed in a bath with stirring at the temperature of 90 °C for 10 h. After the flask was cooled down, the precipitate was centrifuged and then washed several times with deionized water. Finally, the precipitate was dried in an oven at 105 °C for 24 h [31].

### 2.2. Characterization

X-ray diffraction (XRD) analysis was carried out on a Rigaku D/max-2400 X-ray diffractometer with  $Cu K\alpha$  radiation ( $\lambda = 1.5406 \text{ \AA}$ ). Transmission electron microscopy (TEM) analysis was conducted on a JEOL 2011 transmission electron microscope (JEOL, Japan) with an accelerating voltage of 150 kV. Raman spectra were carried out using a microscopic confocal Raman spectrometer HORIBA HR 800 with an excitation of 514 nm laser light. The active species of phenol degradation by  $MnO_2$  structure catalyst can be detected on Bruker EPR 300E electronic paramagnetic resonance spectrometer using DMPO (5, 5-dimethyl-1-pyrroline *N*-oxide) as free radical trapping agent.

### 2.3. Catalytic degradation experiment

The degradation reactions were carried out with a 50 mL 5 ppm phenol solution and 25 mg catalyst powders. The suspension solution was first ultrasonic dispersed in dark for 15 min and then magnetically stirred for 1 h to reach the adsorption-desorption equilibrium. At given time intervals, 4 mL solution were sampled and centrifuged to remove the catalysts. The concentration of phenol contaminants was analysed by Shimadzu LC-20A high performance liquid chromatography (HPLC) with a Venusil XBP-C18 and a UV detector operated at 270 nm. Venusil XBPC18 (250 mm  $\times$  4.6 mm 5  $\mu$ m) reversed phase column was used. The mobile phase consisted of methanol and water (volume ratio: 55/45) at a flow rate of 1 mL/min.

### 2.4. Computational method

Our calculations were based on the density functional theory (DFT) with the Perdew–Burke–Ernzerhof [32] version of the generalized gradient approximation (GGA-PBE) for the exchange–correlation potential, as implemented in a plane-wave basis code VASP [33,34,49]. The pseudo-potential was described by the projector-augmented-wave (PAW) method [35]. In both bulk and surface calculations, the geometry optimization is performed until the Hellmann–Feynman force on each atom is smaller than  $0.02 \text{ eV \AA}^{-1}$  during the atomic structure optimization. The atoms were relaxed and re-optimized with a conjugate gradient (CG) [36] method. The numerical integration in the first Brillouin zone is performed using a Monkhorst–Pack grid of  $7 \times 7 \times 3$  for the bulk, and  $3 \times 3 \times 1$  for the surface, respectively. To check the convergence, we have compared the total energy to the ones calculated with finer k-mesh. The difference is smaller than 5 meV.

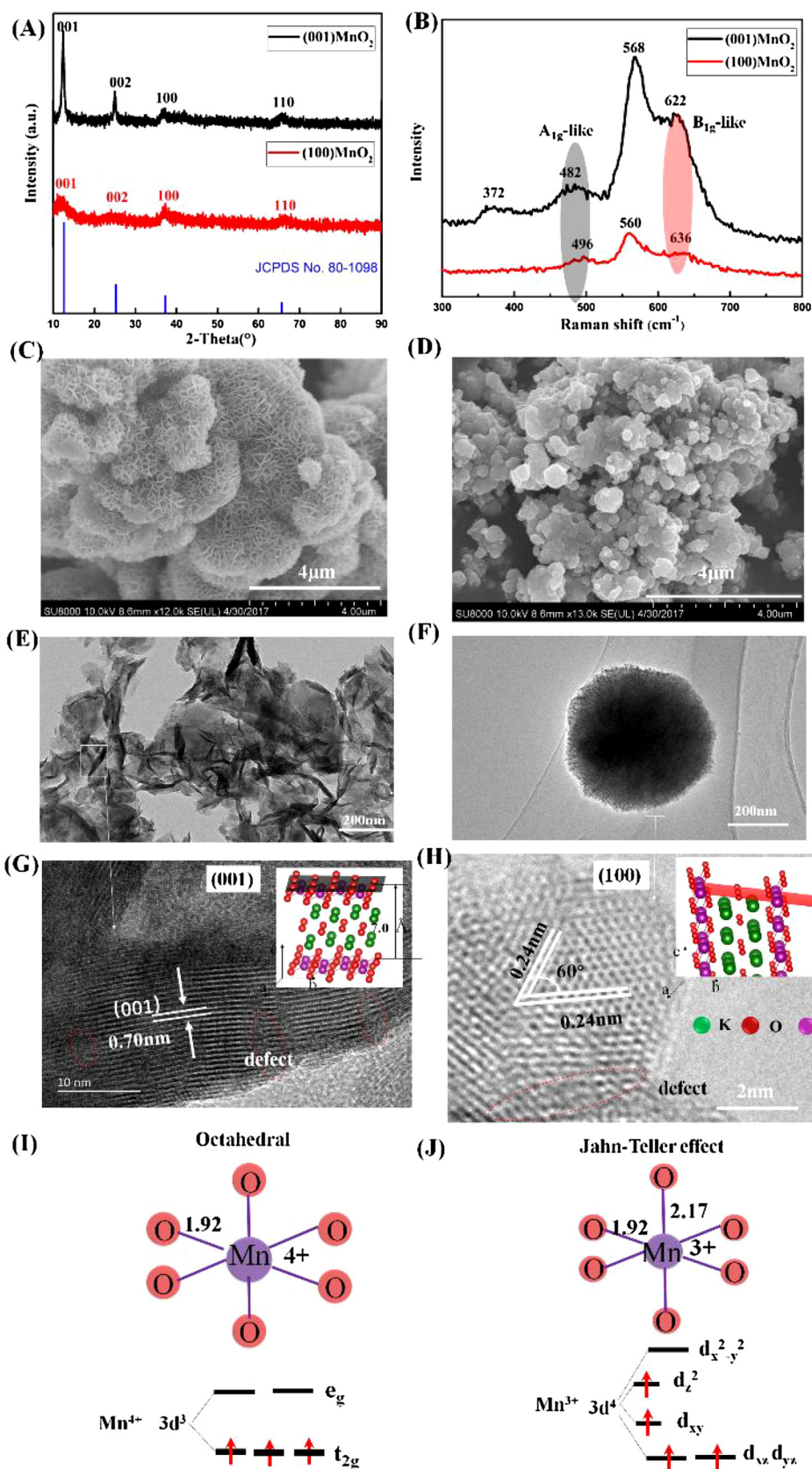


**Fig. 1.** (A) XRD pattern (B) Raman (C) and (D) SEM (E) and (F) TEM, (G) and (H) HRTEM of (001) MnO<sub>2</sub> and (100) MnO<sub>2</sub> with atom structure of MnO<sub>2</sub>, (I) (J) is the octahedral structure of MnO<sub>2</sub> with Mn<sup>4+</sup> electronic orbital and Jahn-Teller effect with Mn<sup>3+</sup> electronic orbital. For the Mn<sup>3+</sup>, the Jahn-Teller effect causes elongation of Mn-O bond compared to Mn<sup>4+</sup>.



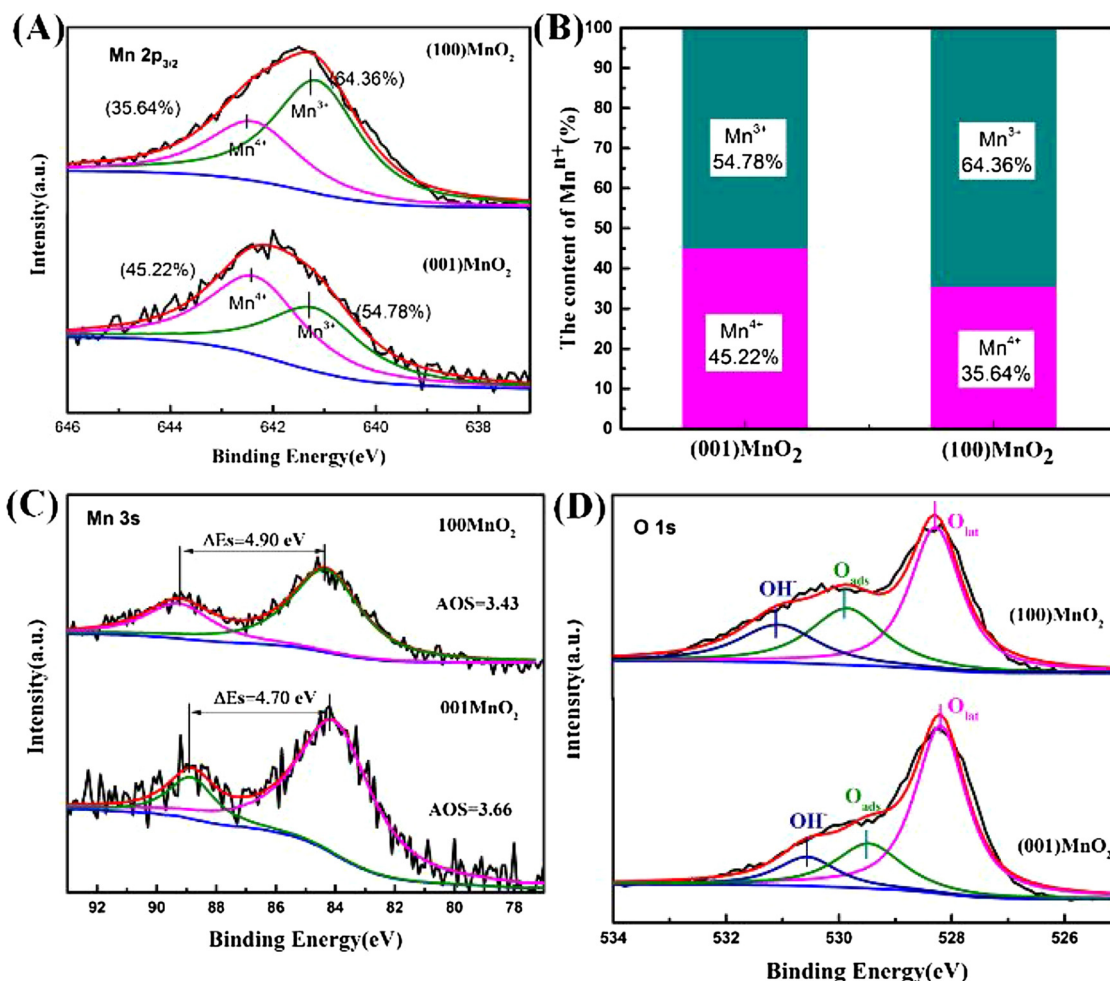


Fig. 2. High-resolution XPS spectra of (001) MnO<sub>2</sub> and (100) MnO<sub>2</sub>: (A) Mn 2p<sub>3/2</sub>, (B) the content of Mn<sup>n+</sup>, (C) Mn 3s and (D) O 1s.

We optimized a monoclinic birnessite (C12/m1) with lattice constants  $a = 5.149 \text{ \AA}$ ,  $b = 2.842 \text{ \AA}$  and  $c = 7.047 \text{ \AA}$ , which are in good agreement with the experimental value of  $a = 5.149 \text{ \AA}$ ,  $b = 2.843 \text{ \AA}$  and  $c = 7.176 \text{ \AA}$ . To overcome the inaccuracy of standard DFT in describing the partially filled d-states in Mn<sup>3+</sup> ions, we used GGA + U formalism to correct the on-site Coulomb and exchange interactions for localized d orbitals. We adopted the values of  $U - J = 5.10 \text{ eV}$  and  $J = 1.00 \text{ eV}$  according to the literature [37]. Spin is considered to optimize the structures.

The oxygen vacancy energy ( $E_{OV}$ ) is one of great important quantity to describe activity of exposed oxide surfaces. In the current work,  $E_{OV}$  is calculated using the following formula:  $E_{OV} = E_{\text{sys-O}} - E_{\text{sys}} + E_{O2}/2$

Where  $E_{\text{sys}}$  and  $E_{\text{sys-O}}$  are the total energies of ideal and defective (with one oxygen vacancy) birnessite MnO<sub>2</sub> slabs, respectively.

### 3. Results and discussion

#### 3.1. Structure characterization

Fig. 1 (A) presents the XRD pattern of birnessite-type MnO<sub>2</sub> with (001) and (100) exposed faces. Peak locates at 12.3°, 24.6°, 36.5° and 65.5° which agrees well with (001), (002), (100) and (110) of MnO<sub>2</sub> (JCPDS No. 80-1098). The structure consists of single sheets of edge-sharing [MnO<sub>6</sub>] octahedral layer and water molecules and K<sup>+</sup> between the layers. The orthogonal distance between two consecutive slabs of [MnO<sub>6</sub>] is ca. 7.0 Å. For (001) MnO<sub>2</sub>, the first characteristic peak at 12.3° shows high intensity in comparison with other planes, illustrating (001) plane shows long-range order and exposes great quantities. While 36.5°

peak shows enhanced intensity compared with 12.3° peak for (100) MnO<sub>2</sub>. Furthermore, the peak width of (100) MnO<sub>2</sub> enlarges illustrating the particle size increases caused by the Jahn-Teller effect. Fig. 1 (B) shows the Raman spectrum of MnO<sub>2</sub> at the irradiation wavelength of 514.5 nm, which is characterized by two sharp peaks at 568 and 622 cm<sup>-1</sup> along with two weak bands at 372 cm<sup>-1</sup> and 482 cm<sup>-1</sup>. The main contributions are assigned to the A<sub>1g</sub> and B<sub>1g</sub> stretching mode of the MnO<sub>6</sub> octahedral. A<sub>1g</sub> reflects compress and stretch vibration, while B<sub>1g</sub> relates to stretch vibration of the Mn–O in MnO<sub>6</sub> octahedral. After analyzing the Raman data, Jahn-Teller effect of (100) MnO<sub>2</sub> is more than that of (001) MnO<sub>2</sub>. In Fig. 1(C), the morphology of (001) MnO<sub>2</sub> showed nanosheet-resemble flower-like structures. In its corresponding TEM characterization of Fig. 1(E), (001) MnO<sub>2</sub> nanosheet curls and overlaps. In its magnified HRTEM of Fig. 1(G), the lattice fringe spacing was ca. 0.70 nm corresponding to the interplanar spacing of the (001) planes of MnO<sub>2</sub>. The crystal structure is closely-packed with exposure of high-density oxygen atoms, which are more thermodynamically stable. (100) MnO<sub>2</sub> consists of nanoparticles aggregation with coarse surface shown in Fig. 1(D) and (F). In its HRTEM of Fig. 1(H), the lattice fringe spacing was ~0.24 nm with a cross angle of 60° corresponding to the (100) planes of the hexagonal layered-structure MnO<sub>2</sub>. The exposed atom mainly consists of potassium atoms, whose radius is nearly twice of that of Mn atoms. (100) MnO<sub>2</sub> has an open channel structure with exposure of potassium (K), manganese (Mn), oxygen (O) atom. Owing to the existence of defect, MnO<sub>2</sub> is converted from a stable d<sup>3</sup> (Mn<sup>4+</sup>) state to unstable high-spin d<sup>4</sup> (Mn<sup>3+</sup>) state. These Mn<sup>3+</sup> cations would have a strong Jahn-Teller effect, elongating a pair of oxygen in order to split d orbitals to fill the lower

energy orbital. With the  $\text{Mn}^{3+}$  number increasing, the layers will be destabilized and the expansion of  $\text{MnO}_6$  layers becomes more pronounced, granting the layers relax by increasing bond lengths as there is less  $\text{Mn}^{4+}$  to resist the elongation of the  $\text{Mn}^{3+}$  bonds. To be more specific, in Fig. 1(I), the ground-state high-spin configured Mn could be regarded as  $t_{2g}^3$  for  $\text{Mn}^{4+}$  and  $d_{xz}^1, d_{yz}^1, d_{xy}^1, d_z^2$  for Joan Teller effect of  $\text{Mn}^{3+}$  in Fig. 1(J), respectively.

### 3.2. Surface chemical states

The activity of the catalyst depends on exposed surficial atoms which could be analyzed by XPS. As shown in Fig. 2(A), the Mn 2p 3/2 peak could be split into two peaks with the binding energy at 642.9 eV and 641.5 eV, corresponding to  $\text{Mn}^{4+}$  and  $\text{Mn}^{3+}$ , respectively. [38] For (001)  $\text{MnO}_2$ , the proportion of  $\text{Mn}^{4+}$  and  $\text{Mn}^{3+}$  is 45.22% and 54.78%, while 35.64% and 64.36% for (100)  $\text{MnO}_2$ . The result shows that the content of  $\text{Mn}^{3+}$  is more for (100)  $\text{MnO}_2$  than that of (001)  $\text{MnO}_2$  in Fig. 2(B), illustrating that (100)  $\text{MnO}_2$  owns more oxygen vacancy concentration [39]. The surface average oxidation state (AOS) of Mn could be calculated according to the following formula [40]:  $\text{AOS} = 8.956 - 1.126\Delta E_s$ , where  $\Delta E_s$  represents the binding energy difference between two Mn 3s peaks. Through calculating the  $\Delta E_s$ , the AOS of Mn could be obtained as 3.66 and 3.43 for (001)  $\text{MnO}_2$  and (100)  $\text{MnO}_2$ , respectively shown in Fig. 2(C). We also investigated the XPS of the (100) $\text{MnO}_2$  after reaction shown in Fig. S7. The result shows that the content of  $\text{Mn}^{3+}$  does not change, while the AOS of Mn increases from 3.43 to 3.89, which all illustrating that Mn does not participate in the reaction and oxygen vacancy participate in the reaction.

Moreover, DFT has been conducted to calculate the oxygen vacancy formation energy. The calculated oxygen vacancy of birnessite  $\text{MnO}_2$  with (001) and (100) crystal plane is 1.45 eV and 1.43 eV, respectively, illustrating that (100) crystal plane is more active than that of the (001) crystal plane for catalytic reactions. The oxygen species on the catalyst surface play a vital role in the catalytic activity, which could be distinguished via the O 1s peak in Fig. 2(D). The O 1s spectra based on the different chemical states could be split and fitting into three peaks: hydroxyls ( $\cdot\text{OH}$ ), adsorption oxygen ( $\text{O}_{\text{ads}}$ ) and lattice oxygen ( $\text{O}_{\text{lat}}$ ) [41]. Notably, (100)  $\text{MnO}_2$  presents the higher ratio of adsorption oxygen ( $\text{O}_{\text{ads}}$ ) or hydroxyls ( $\cdot\text{OH}$ ) than that of (001)  $\text{MnO}_2$ , owing to its potential moderate interaction with adsorbed oxygen or  $\text{H}_2\text{O}$  species contributed by  $\text{Mn}^{3+}$  with  $dz^2$  orbital.

The catalytic reaction usually took place at the surface oxygen vacancy which works as an active center or  $\text{O}_2$  adsorption site [42]. Intrinsic and intact  $\text{MnO}_2$  structure is illustrated in Fig. 3(A) with its density of states (DOS) in Fig. 3(B). Semiconductor properties could be available from the analysis of the DOS with spin orbital up and spin orbital down. The relaxed structure of (001)  $\text{MnO}_2$  with defect is shown in Fig. 3(C) with a black circle representing an oxygen vacancy. The corresponding DOS was also calculated, which shows half-metallicity characteristics with hybrid bands near the E-fermi shown in Fig. 3(D). While the (100)  $\text{MnO}_2$  with oxygen vacancy shows half-metallicity characteristics with band gap nearly zero, which favors excellent electrical conductivity, efficient electron transport and ion diffusion properties shown in Fig. 2(J). The DOS difference between (001)  $\text{MnO}_2$  and (100)  $\text{MnO}_2$  implies the latter shows better phenol degradation rate and content than the former owing to its continuous band gap.

### 3.3. Active species

To confirm active species on the catalyst  $\text{MnO}_2$  surface, the EPR technique was carried out with DMPO as an electron trapping agent. In Fig. 4(A), there is no any signal for pure  $\text{MnO}_2$  and  $\text{MnO}_2$  in water solution. While for (001)  $\text{MnO}_2$  in water solution adding DMPO as an electron trapping agent at the temperature of 15 °C and 25 °C, four characteristic peaks with relative intensities of 1: 2: 2: 1 could be obviously observed, which could be ascribed to DMPO-OH adduct,

consistent with DFT calculation of water dissociative adsorbing in Fig. S6. Additionally, for (001) $\text{MnO}_2$  in water solution at the temperature of 40 °C and 55 °C, two sets of peaks could be observed, which could be assigned to  $\cdot\text{OH}$  and  $\cdot\text{O}_2^-$ . What's more, the simulation curve of (001)  $\text{MnO}_2$  in water solution at the temperature of 40 °C consists of  $\cdot\text{OH}$  and  $\cdot\text{O}_2^-$ , which is consistent with experiment observation shown in Fig. 4(B), illustrating that active species could be generated and transformed via adjusting the temperature. In order to shed light on the deeper reason for the different active species, atomic-scale interaction behaviors between the oxygen vacancies and  $\text{O}_2$  analysis is also conducted based on above comprehensive atomic level understanding of oxygen vacancies geometric and electronic structure. The geometric structure of  $\text{O}_2$  adsorbed on (001)  $\text{MnO}_2$  surface is first optimized with the adsorption height beyond chemisorption. However, a systematically investigation of the  $\text{O}_2$  adsorption on the  $\text{MnO}_2$  with oxygen vacancy showed dissimilar and interesting phenomenon. If  $\text{O}_2$  gas stands at the top of or lies around  $\text{Mn}^{3+}$  ions close to the surface oxygen vacancy,  $\text{O}_2$  gas would slip into the surface vacancy and bind to two nearest unsaturated  $\text{Mn}^{3+}$  cation in the sublayers which is the most reliable sites via a Lewis acid interaction to form an end-on structure shown in Fig. S5. The O–O bond length in the structures was activated to 1.23 Å, which is close to that of  $\cdot\text{O}_2^-$  (1.26 Å) in Fig. 4(D). One redistributed 4f electron of  $\text{Mn}^{3+}$  ions feedback to the  $\pi 2py^*$  orbital of O, a superoxide species form which is in accordance with the calculated one-electron transfer in the Bader charge. To further identify the oxygen species above, the corresponding orbital is shown in Fig. 4(D) with one-electron at the outmost  $\pi 2py^*$  orbital. In Fig. 4(E), there are no any peaks for pure (100)  $\text{MnO}_2$  powder and (100)  $\text{MnO}_2$  in water solution without DMPO as an electron trapping agent. Whereas a typical seven-line paramagnetic signal is detected for  $\text{MnO}_2$  in water with DMPO at the temperature of 15 °C, 25 °C and 40 °C, which can be ascribed to DMPO- $\text{O}_2^{2-}$  (or  $\text{H}_2\text{O}_2$ ). [43–46] In addition, the intensity of the  $\text{O}_2^{2-}$  peaks is enhancing distinctly from 15 °C to 40 °C. We integrated the area of  $\text{O}_2^{2-}$  and Mn standard signals and obtained the  $\text{O}_2^{2-}$  concentration relationship with temperature shown in Fig. 4(F). The  $\text{O}_2^{2-}$  concentration changes with the increasing temperature of (100)  $\text{MnO}_2$ , which implied that raising temperature favors the generation rate and further increasing the amount of  $\text{O}_2^{2-}$ . The adsorption of  $\text{O}_2$  on the oxygen vacancy of (100)  $\text{MnO}_2$  surface by combining with three nearest potassium (K) atoms in the outset layer to form a complex end-on configuration. Interesting, the O–O bond length of  $\text{O}_2$  was weakened to 1.46 Å, close to the bond lengths of  $\text{O}_2^{2-}$  or  $\text{H}_2\text{O}_2$  active species (1.49 Å) in Fig. 4(G). Two 4f electrons of  $\text{Mn}^{3+}$  ions in the Bader charge feedback to the  $\pi 2py^*$  orbital of O, a peroxide species  $\text{O}_2^{2-}$  form at the crystal plane of birnessite (100)  $\text{MnO}_2$ . To further recognize the oxygen species, the corresponding orbital is shown in Fig. 4(H) with two electrons at the outmost  $\pi 2py^*$  orbital. The DFT result of oxygen active species is consistent with experimental spin-trapping EPR observation. It was therefore concluded that peculiar interaction between oxygen vacancies of  $\text{MnO}_2$  and  $\text{O}_2$  favored  $\text{O}_2$  activation and generation of  $\cdot\text{O}_2^-$  or  $\text{O}_2^{2-}$ , which results in facet-dependent oxygen activation on birnessite  $\text{MnO}_2$ .

### 3.4. Catalytic activity

In order to investigate the  $\text{MnO}_2$  degradation of phenol at a controlled constant environment temperature range from 30 °C to 80 °C, both (100) and (001)  $\text{MnO}_2$  shows enhanced phenol degradation performance with temperature increasing. Note that phenol solution in the absence of catalyst nearly does not result in the catalytic decomposition at the temperature of 30 °C and 40 °C, while phenol concentration decreased by 18% at the temperature of 80 °C shown in Fig. S1. Therefore, the presence of a catalyst is necessary for efficient degradation. To evaluate the catalytic efficiency quantitatively, the degradation rate constants (k) were obtained by fitting the lines of  $\ln(C_0/C)$  vs. t, assuming that the chemical reaction follows pseudo first-order kinetics

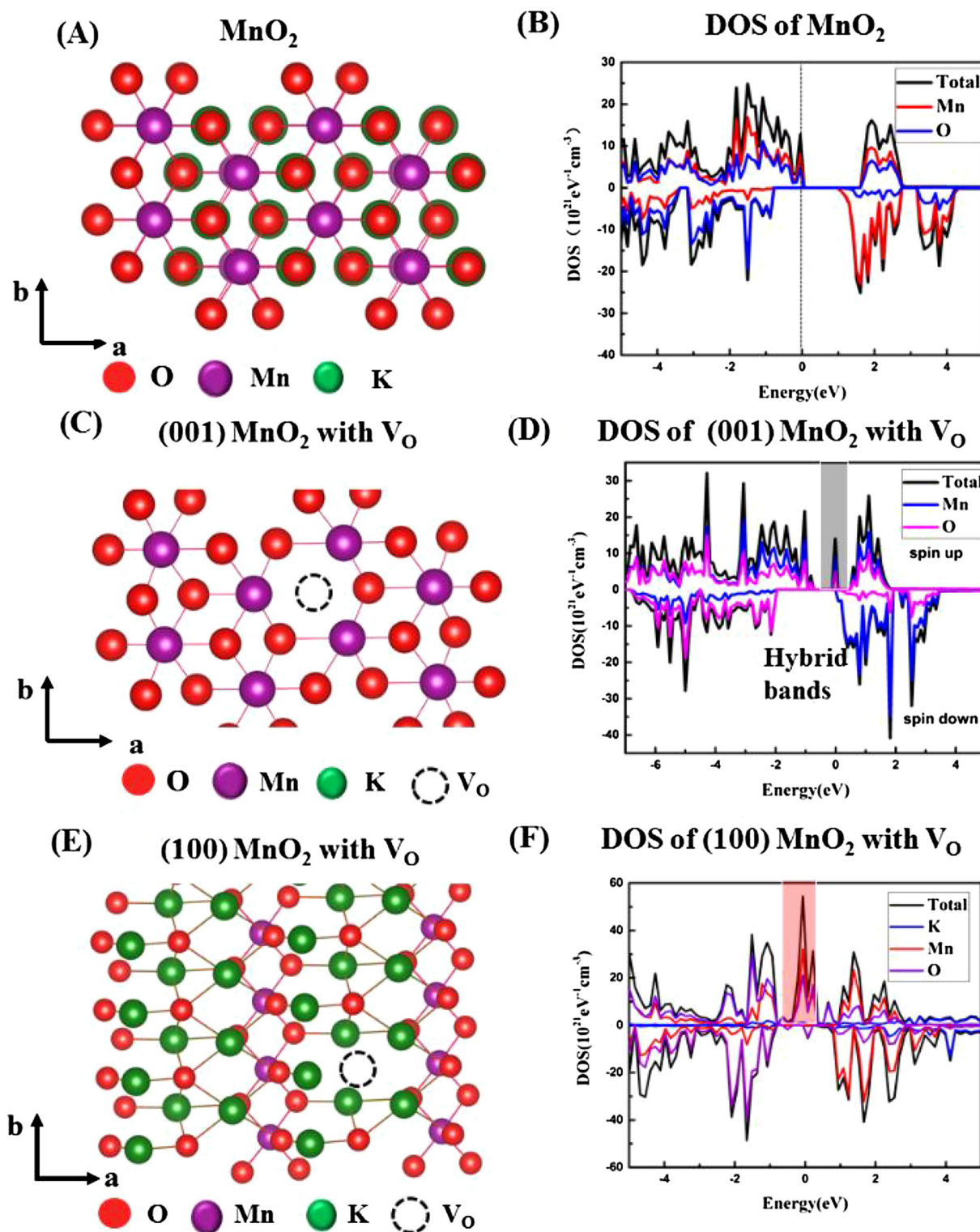


Fig. 3. Top view of pure birnessite-type MnO<sub>2</sub> and corresponding density of states (DOS) (A, B), oxygen vacancy configurations and corresponding DOS of (001) MnO<sub>2</sub> (C, D) and (100) MnO<sub>2</sub> (E, F).

(where C means the concentration of solute remaining in the solution at the irradiation time of t and C<sub>0</sub> refers to the initial solution concentration). Accordingly, the reaction rate constants of (001) MnO<sub>2</sub> and (100) MnO<sub>2</sub> is increasing with the temperature rising shown in Fig. 5(A) and (B). Interestingly (100) MnO<sub>2</sub> shows faster degradation phenol rate than that of (001) MnO<sub>2</sub>. Phenol conversion ratio could be also calculated through the formula: Conversion (%) = [(C<sub>0</sub> - C)/C<sub>0</sub>] × 100; The result shows that (100) MnO<sub>2</sub> shows more phenol

degradation content than that of (001) MnO<sub>2</sub> shown in Fig. 5(C) and (D). For (100) MnO<sub>2</sub>, phenol conversion ratio is 14.5% and 80.6% at the temperature of 30 °C and 60 °C shown in Fig. 5(E). In order to access phenol mineralization content, total organic carbon analyzer (TOC) is conducted to evaluate the degree of mineralization phenol of the MnO<sub>2</sub> (100). Fig. 5(F) shows the degree of mineralization by the same catalyst is 10% and near 37.5% after 3 h at the temperature of 30 °C and 60 °C. According to the Arrhenius formula [47]  $\ln k = \ln A - E_a/RT$ , the



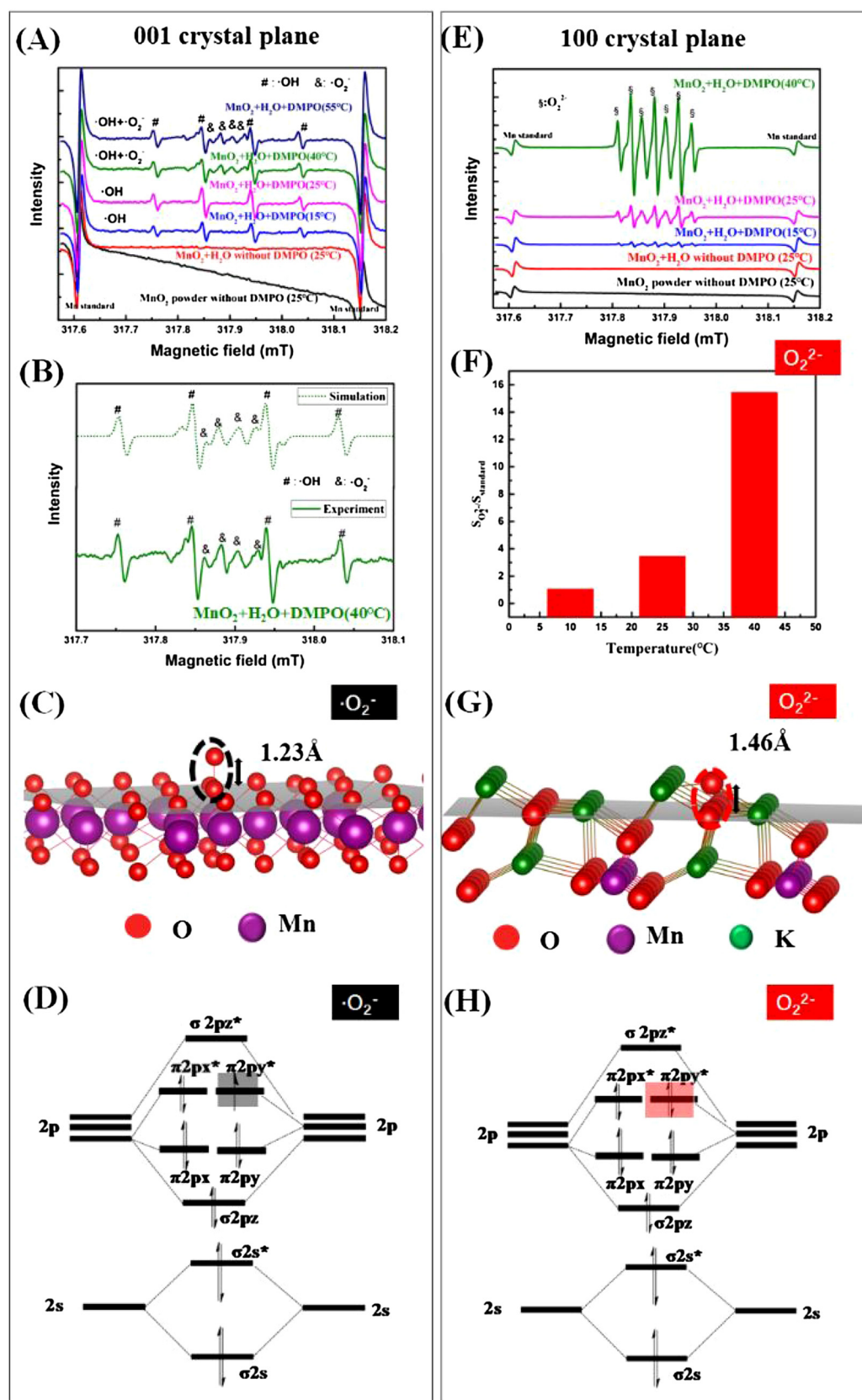


Fig. 4. Typical EPR spectra of active oxygen radicals on (001)  $\text{MnO}_2$  (A) and (100)  $\text{MnO}_2$  (E) powder without adding DMPO,  $\text{MnO}_2$  in water solution without DMPO and in the presence of DMPO as an electron trapping agent at the temperature of 15 °C, 25 °C, 40 °C and 55 °C. The simulation and experiment curve of (001)  $\text{MnO}_2$  with DMPO at the temperature of 40 °C (B). The atomic model of  $\text{O}_2$  adsorbed on (001)  $\text{MnO}_2$  with chemical bond length of 1.23 Å, indicating  $\cdot\text{O}_2^-$  active species (C). The corresponding molecule orbital of  $\cdot\text{O}_2^-$  with outset  $\pi 2p_y^*$  orbital of one electron (D). The  $\text{O}_2^{2-}$  concentration changes with the increasing temperature on (100)  $\text{MnO}_2$  (F). The atomic model of  $\text{O}_2$  adsorbed on (100)  $\text{MnO}_2$  with chemical bond length of 1.46 Å, indicating  $\text{O}_2^{2-}$  (G) active species. The corresponding molecule orbital of  $\text{O}_2^{2-}$  (H) with outset  $\pi 2p_y^*$  orbital of two electrons.

apparent activation energy ( $E_a$ ) could be then calculated via the slope of the linear fit of the ( $1000/T$ ,  $\ln k$ ) plot. The calculated  $E_a$  of (100)  $\text{MnO}_2$  and (001)  $\text{MnO}_2$  is 49.05 KJ/mol and 60.80 KJ/mol, respectively, illustrating that (100)  $\text{MnO}_2$  could effectively lower the reaction active

energy than that of (001)  $\text{MnO}_2$  shown in Fig. 5(G). We also analyzed the catalytic intermediate species of phenol over  $\text{MnO}_2$  (001) and (100) using HPLC spectrums under 80 °C and room temperature shown in Fig. S2. The intermediate species mainly consist of some small molecules. In

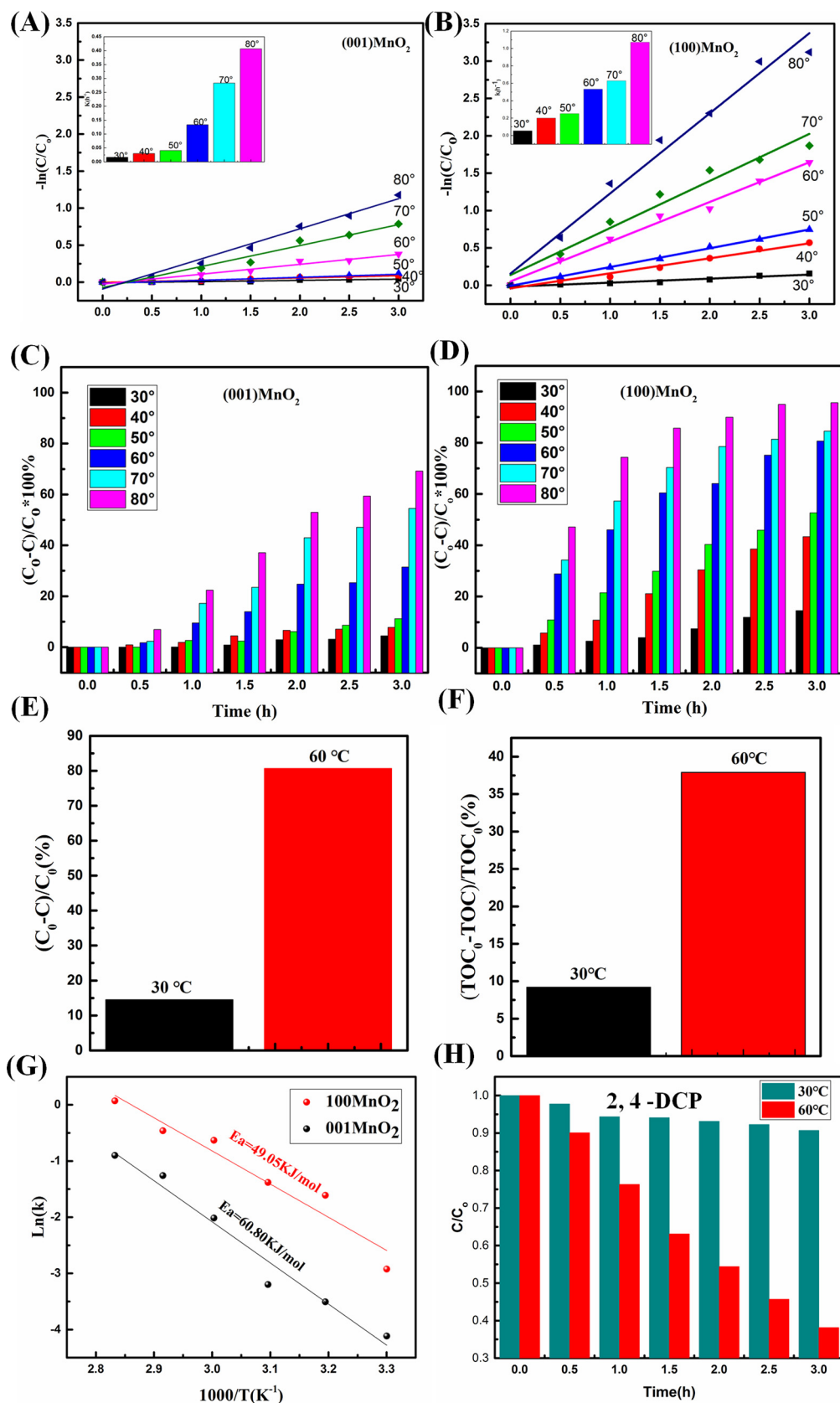


Fig. 5. Thermal-degradation performance on phenol of (001) MnO<sub>2</sub> (A) and (100) MnO<sub>2</sub> (B) at a different temperature. Arrhenius plots for phenol oxidation over (001) MnO<sub>2</sub> and (100) MnO<sub>2</sub> catalysts (C) and mineralization content (D) of phenol of (100) MnO<sub>2</sub> at the temperature of 30 °C and 60 °C.



order to investigate  $\text{MnO}_2$  degradation properties of other phenol-based pollutant, the catalytic degradation performance of 10 ppm 2, 4-DCP used as a typical indicator for (100)  $\text{MnO}_2$  at the temperature of 30 °C and 60 °C shown in Fig. 5 (H). 2, 4-DCP degradation content of  $\text{MnO}_2$  (100) decreased by ~10% and 70% at the temperature of 30 °C and 60 °C after 3 h. In short, (100)  $\text{MnO}_2$  shows high efficiency to degrade and deep mineralize phenol-based pollutant at low temperature.

BHT as superoxide species trapper was added in phenol solution with the result showing that phenol did not degrade compared with pure  $\text{MnO}_2$  shown in Fig. S4. The  $\text{O}_2$  molecule may attack oxygen vacancy on the surface of (001)  $\text{MnO}_2$ , leading to the formation of the superoxo species ( $\cdot\text{O}_2^-$ ) shown in Fig. S5. The superoxo species sequent transforms into surface hydroxyl  $\text{MnOH}$  shown in Fig. S6. The resultant active species hydroxyl radicals ( $\cdot\text{OH}$ ) immediately react with phenol in the ortho position to form hydroquinone. The compound is further oxidized to produce benzoquinone with mass spectrometry analysis shown in Fig. S3, which is hydroxylated and eventually forms lower molecular weight carbon dioxide and water [48]. On (100)  $\text{MnO}_2$ , the  $\text{O}_2$  molecule may occupy oxygen vacancy on the surface of (100)  $\text{MnO}_2$ , leading to the formation of peroxide species  $\text{O}_2^{2-}$  shown in Fig. 4(G) with the strong oxidization ability, which would react with phenol which ultimately oxidize into carbon dioxide and water. The active species superoxide radical ( $\cdot\text{O}_2^-$ ), hydroxyls ( $\cdot\text{OH}$ ) on (001)  $\text{MnO}_2$  and peroxide radical ( $\text{O}_2^{2-}$ ) on (100)  $\text{MnO}_2$  might account for the difference of phenol degradation properties. Peroxide radical ( $\text{O}_2^{2-}$ ) rationalize the lowered phenol degradation activation energy barrier, and enhance the phenol degradation content and mineralization ability through comparing with superoxide radical ( $\cdot\text{O}_2^-$ ) and hydroxyls ( $\cdot\text{OH}$ ). The active species superoxide radical ( $\cdot\text{O}_2^-$ ), hydroxyls ( $\cdot\text{OH}$ ) on (001)  $\text{MnO}_2$  and peroxide radical ( $\text{O}_2^{2-}$ ) on (100)  $\text{MnO}_2$  might account for the difference of phenol degradation properties.

#### 4. Conclusion

Birnessite-type  $\text{MnO}_2$  with (001) and (100) crystal planes were successfully fabricated experimentally using the hydrothermal and water bath method. There are 3 times faster catalytic degradation phenol rate, 11 KJ/mol reduced activation energy and ~30% degradation content of catalytic reaction of (100)  $\text{MnO}_2$  than that of (001)  $\text{MnO}_2$ . Spin-trapping EPR technique was carried out to detect the active species superoxide radical ( $\cdot\text{O}_2^-$ ) and hydroxyls ( $\cdot\text{OH}$ ) on (001)  $\text{MnO}_2$ , and peroxide radical ( $\text{O}_2^{2-}$ ) on (100)  $\text{MnO}_2$ . Additionally, only hydroxyls ( $\cdot\text{OH}$ ) exists when the temperature is lower than 40 °C, while  $\cdot\text{OH}$  and  $\cdot\text{O}_2^-$  could coexist on (001)  $\text{MnO}_2$  at the temperature higher than 40 °C. The amount of  $\text{O}_2^{2-}$  is enhancing with temperature increasing for (100)  $\text{MnO}_2$ . Moreover, DFT calculation result shows that superoxide species form on the (001)  $\text{MnO}_2$  with O–O bond length of 1.23 Å. Peroxide species are obtained with O–O bond length of 1.44 Å, which is in agreement with the EPR results. The comprehensive understanding of oxygen vacancy and ROS enables to help consolidate and strengthen the fundamental theories of catalysis, more importantly provide new guidelines for the rational design of highly efficient catalysts.

#### Acknowledgements

This work was partly supported by Chinese National Science Foundation (21437003, 21673126, 21761142017, 21621003, 51651201, 11641002), collaborative Innovation Center for Regional Environmental Quality, and the Science and Technology Department of Shaanxi Province (2016KTZDGY04-03) and the high-level personnel research funds in Yulin University (16GK13). We are grateful to Ms. Xixi Liang (Tsinghua University) for her help on the EPR measurements. Our work is completed on the “Explorer 100” cluster system of Tsinghua National Laboratory for Information Science and Technology.

#### Appendix A. Supplementary data

Supplementary material related to this article can be found, in the online version, at doi:<https://doi.org/10.1016/j.apcatb.2018.03.107>.

#### References

- [1] E. Wahlström, E.K. Vestergaard, R. Schaub, et al., Electron transfer-induced dynamics of oxygen molecules on the  $\text{TiO}_2$  (110) surface, *Science* 303 (2004) 511–513.
- [2] M. Setvín, U. Aschauer, P. Scheiber, et al., Reaction of  $\text{O}_2$  with subsurface oxygen vacancies on  $\text{TiO}_2$  anatase (101), *Science* 341 (2013) 988–991.
- [3] S. Tan, Y. Ji, Y. Zhao, et al., Molecular oxygen adsorption behaviors on the rutile  $\text{TiO}_2(110)-1 \times 1$  surface: an in situ study with low-temperature scanning tunneling microscopy, *J. Am. Chem. Soc.* 133 (2011) 2002–2009.
- [4] C. Li, K. Domen, K. Maruya, T. Onishi, Dioxxygen adsorption on well-outgassed and partially reduced cerium oxide studied by FT-IR, *J. Am. Chem. Soc.* 111 (1989) 7683–7687.
- [5] Y. Zhao, B.T. Teng, X.D. Wen, et al., Superoxide and peroxide species on  $\text{CeO}_2(111)$ , and their oxidation roles, *J. Phys. Chem. C* 116 (2012) 15986–15991.
- [6] H. Gerischer, A. Heller, Photocatalytic oxidation of organic molecules at  $\text{TiO}_2$  particles by sunlight in aerated water, *J. Electrochem. Soc.* 139 (1992) 113–118.
- [7] C.M. Wang, A. Heller, H. Gerischer, Palladium catalysis of  $\text{O}_2$  reduction by electrons accumulated on  $\text{TiO}_2$  particles during photoassisted oxidation of organic compounds, *J. Am. Chem. Soc.* 114 (1992) 5230–5234.
- [8] Y. Li, W. Zhang, J.F. Niu, Y.S. Chen, Mechanism of photogenerated reactive oxygen species and correlation with the antibacterial properties of engineered metal-oxide nanoparticles, *ACS Nano* 6 (2012) 5164–5173.
- [9] M.A. Henderson, I. Lyubintsev, Molecular-Level insights into photocatalysis from scanning probe microscopy studies on  $\text{TiO}_2(110)$ , *Chem. Rev.* 113 (2013) 4428–4455.
- [10] E. Wahlström, E.K. Vestergaard, R. Schaub, A. Ronnau, M. Vestergaard, E. Lagsgaard, I. Stensgaard, F. Besenbacher, Electron transfer-induced dynamics of oxygen molecules on the  $\text{TiO}_2$  (110) surface, *Science* 303 (2004) 511–513.
- [11] N.G. Petrik, G.A. Kimmel, Oxygen photochemistry on  $\text{TiO}_2$  (110): recyclable, photoactive oxygen produced by annealing adsorbed  $\text{O}_2$ , *J. Phys. Chem. Lett.* 2 (2011) 2790–2796.
- [12] U. Aschauer, J. Chen, A. Selloni, Peroxide and superoxide states of adsorbed  $\text{O}_2$  on anatase  $\text{TiO}_2$  (101) with subsurface defects, *Phys. Chem. Chem. Phys.* 12 (2010) 12956–12960.
- [13] Z.T. Wang, Y.G. Du, Z. Dohnalek, I. Lyubintsev, Direct observation of site-specific molecular chemisorption of  $\text{O}_2$  on  $\text{TiO}_2(110)$ , *J. Phys. Chem. Lett.* 1 (2010) 3524–3529.
- [14] A. Tiloca, A. Selloni,  $\text{O}_2$  and vacancy diffusion on rutile (110): pathways and electronic properties, *ChemPhysChem* 6 (2005) 1911–1916.
- [15] S. Tan, Y. Ji, Y. Zhao, A. Zhao, B. Wang, J. Yang, J.G. Hou, Molecular oxygen adsorption behaviors on the rutile  $\text{TiO}_2(110)-1 \times 1$  surface: an in situ study with low-temperature scanning tunneling microscopy, *J. Am. Chem. Soc.* 133 (2011) 2002–2009.
- [16] L. Lan, Y.Z. Li, M. Zeng, M.Y. Mao, L. Ren, Y. Yang, H.H. Liu, L. Yun, X.J. Zhao, Efficient UV–vis-infrared light-driven catalytic abatement of benzene on amorphous manganese oxide supported on anatase  $\text{TiO}_2$  nanosheet with dominant {001} facets promoted by a photothermocatalytic synergetic effect, *Appl. Catal. B Environ.* 203 (2017) 494–504.
- [17] Y. Yang, Y.Z. Li, M.Y. Mao, M. Zeng, X.J. Zhao, UV–Visible–Infrared light driven thermocatalysis for environmental purification on ramsdellite  $\text{MnO}_2$  hollow spheres considerably promoted by a novel photoactivation, *ACS Appl. Mater. Interfaces* 9 (2017) 2560–2571.
- [18] Y. Yuan, C. Zhan, K. He, et al., The influence of large cations on the electrochemical properties of tunnel-structured metal oxides, *Nat. Commun.* 7 (2016) pp13374.
- [19] D.A. Tompsett, S.C. Parker, M.S. Islam, Surface properties of  $\alpha\text{-MnO}_2$ : relevance to catalytic and supercapacitor behavior, *J. Mater. Chem. A* 2 (37) (2014) 15509–15518.
- [20] D.A. Tompsett, S.C. Parker, M.S. Islam, Rutile ( $\beta$ )- $\text{MnO}_2$  surfaces and vacancy formation for high electrochemical and catalytic performance, *J. Am. Chem. Soc.* 136 (2014) 1418–1426.
- [21] H. Wang, J. Zhang, X. Hang, X. Zhang, J. Xie, B. Pan, Y. Xie, Half-Metallicity in single-layered manganese dioxide nanosheets by defect engineering, *Angew. Chem.* 127 (2015) 1211–1215.
- [22] J.L. Wang, J.G. Li, C.J. Jiang, P. Zhou, P.Y. Zhang, J.G. Yu, The effect of manganese vacancy in birnessite-type  $\text{MnO}_2$  on room-temperature oxidation of formaldehyde in air, *Appl. Catal. B Environ.* 204 (2017) 147–155.
- [23] J. Wang, G. Zhang, P. Zhang, Layered birnessite-type  $\text{MnO}_2$  with surface pits for enhanced catalytic formaldehyde oxidation activity, *J. Mater. Chem. A* 5 (2017) 5719–5725.
- [24] A.T. Bell, The impact of nanoscience on heterogeneous catalysis, *Science* 299 (2003) 1688–1691.
- [25] G. Ertl, Reactions at surfaces: from atoms to complexity (nobel lecture), *Angew. Chem. Int. Ed.* 47 (2008) 3524–3535.
- [26] K. An, G.A. Somorjai, Size and shape control of metal nanoparticles for reaction selectivity in catalysis, *ChemCatChem* 4 (2012) 1512–1524.
- [27] H. Wang, J. Zhang, X. Hang, X. Zhang, J. Xie, B. Pan, Y. Xie, Half-Metallicity in single-layered manganese dioxide nanosheets by defect engineering, *Angew. Chem.* 127 (2015) 1211–1215.

- [28] N. Sakai, Y. Ebina, K. Takada, et al., Photocurrent generation from semiconducting manganese oxide nanosheets in response to visible light, *J. Phys. Chem. B* 109 (2005) 9651–9655.
- [29] X.H. Li, G. Ma, Ceder, et al., Direct visualization of the Jahn–Teller effect coupled to Na ordering in Na<sub>5</sub>/8MnO<sub>2</sub>, *Nat. Mater.* 13 (2014) 586–592.
- [30] D. Kwon, K. Refson, G. Sposito, Defect-induced photoconductivity in layered manganese oxides: a density functional theory study, *Phys. Rev. Lett.* 100 (2008) 146601.
- [31] J. Wang, P. Zhang, J. Li, et al., Room-temperature oxidation of formaldehyde by layered manganese oxide: effect of water, *Environ. Sci. Technol.* 49 (2015) 12372–12379.
- [32] J.P. Perdew, K. Burke, M. Ernzerhof, Generalized gradient approximation made simple, *Phys. Rev. Lett.* 77 (1996) 3865 <https://doi.org/PRLTAO> <https://doi.org/10.1103>.
- [33] G. Kresse, J. Furthmüller, Efficient iterative schemes for ab initio total-energy calculations using a plane-wave basis set, *Comp. Mater. Sci.* 6 (1996) 15–50.
- [34] G. Kresse, J. Furthmüller, Efficient iterative schemes for ab initio total-energy calculations using a plane-wave basis set, *Phys. Rev. B* 54 (1996) 11169.
- [35] P.E. Blöchl, Projector augmented-wave method, *Phys. Rev. B* 50 (1994) 17953.
- [36] W.H. Press, B.P. Flannery, S.A. Teukolsky, W.T. Vetterling, *Numerical Recipes*, Cambridge University Press, 1986, pp. 300–307.
- [37] D.A. Tompsett, S.C. Parker, M.S. Islam, Rutile (β-)MnO<sub>2</sub> surfaces and vacancy formation for high electrochemical and catalytic performance, *J. Am. Chem. Soc.* 136 (2014) 1418–1426.
- [38] F. Shi, F. Wang, H. Dai, J. Dai, J. Deng, Y. Liu, G. Bai, K. Ji, C.T. Au, Rod-, flower-, and dumbbell-like MnO<sub>2</sub>: highly active catalysts for the combustion of toluene, *Appl. Catal. A Gen.* 433 (2012) 206–213.
- [39] J. Hou, Y. Li, L. Liu, L. Ren, X. Zhao, Effect of giant oxygen vacancy defects on the catalytic oxidation of OMS-2 nanorods, *J. Mater. Chem. A* 1 (2013) 6736–6741.
- [40] Y. Yang, J. Huang, S. Wang, S. Deng, B. Wang, G. Yu, Catalytic removal of gaseous unintentional POPs on manganese oxide octahedral molecular sieves, *Appl. Catal. B Environ.* 142 (2013) 568–578.
- [41] J.B. Jia, P.Y. Zhang, L. Chen, Catalytic decomposition of gaseous ozone over manganese dioxides with different crystal structures, *Appl. Catal. B: Environ.* 189 (2016) 210–218.
- [42] R. Schaub, P. Thostrup, N. Lopez, E. Lægsgaard, I. Stensgaard, J.K. Nørskov, F. Besenbacher, Oxygen vacancies as active sites for water dissociation on rutile TiO<sub>2</sub> (110), *Phys. Rev. Lett.* 87 (2001) 266104.
- [43] V. Brezova, D. Dvoranova, A. Stasko, Characterization of titanium dioxide photo-activity following the formation of radicals by EPR spectroscopy, *Res. Chem. Intermed.* 33 (2007) 251–268.
- [44] F.A. Villamena, J.K. Merle, C.M. Hadad, J.L. Zweier, Superoxide radical anion adduct of 5,5-Dimethyl-1-pyrroline N-Oxide (DMPO).2. The thermodynamics of decay and EPR spectral properties, *J. Phys. Chem. A* 109 (2005) 6089–6098.
- [45] R.G. Li, Y.X. Weng, X. Zhou, X.L. Wang, Y. Mi, R.F. Chong, H.X. Han, Can Li, Achieving overall water splitting using titanium dioxide-based photocatalysts of different phases, *Energy Environ. Sci.* 8 (2015) 2377–2382.
- [46] S. Chen, D. Yong, X. Zhang, S. Li, W. Shao, Y. Xie, Giant electron–hole interactions in confined layered structures for molecular oxygen activation, *J. Am. Chem. Soc.* 139 (2017) 4737–4742.
- [47] Y. Liu, P. Zhang, Catalytic decomposition of gaseous ozone over todorokite-type manganese dioxides at room temperature: effects of cerium modification, *Appl. Catal. A Gen.* 530 (2017) 102–110.
- [48] R. Nakamura, A. Imanishi, K. Murakoshi, et al., In situ FTIR studies of primary intermediates of photocatalytic reactions on nanocrystalline TiO<sub>2</sub> films in contact with aqueous solutions, *J. Am. Chem. Soc.* 125 (2003) 7443–7450.
- [49] W.S. Zhang, J. Lin, W.P. Xu, H.H. Fu, G.W. Yang, SCStore: managing scientific computing packages for hybrid system with containers, *Tsinghua Sci. Technol.* 22 (2017) 675–681.